Vorticity generation in compressible multiphase flows

A Ballil, A F Nowakowski[1], S Jolgam and F C G A Nicolleau
Sheffield Fluid Mechanics Group, Department of Mechanical Engineering,
University of Sheffield, Mappin Street, Sheffield S1 3JD, United Kingdom

E-mail: a.f.nowakowski@sheffield.ac.uk

Abstract. The simulations of flows in inhomogeneous media of various physical regimes leading to shock-bubble interactions were performed using a developed numerical code based on a multi-component flow model. The numerical method which considers interfaces represented by contact discontinuities as numerically diffused zones, has been applied to simulate compressible two-phase flows. The approach takes advantage of the inherent numerical diffusion present in solutions. The mathematical formulation of the presented method is obtained after an averaging process of the single phase Navier-Stokes equations and contains the non-conservative equations and non-conservative terms that exist in the model to fulfill the interface condition. The finite volume Godunov-type computational technique, equipped with an approximate Riemann solver for calculating fluxes, is applied to simulate flows in two space dimensions. The approach accounts for pressure non-equilibrium. It resolves interfaces separating compressible fluids and captures the baroclinic source of vorticity generation. A numerically challenging shock bubble interaction problem is investigated to evaluate the effect of the Atwood number and shock wave intensity (various Mach numbers) on the interface evolution and vorticity generation.

1. Introduction

Many engineering processes and systems involve the dynamics of high speed compressible multiphase flows. Good examples of such flows with significant density variations, are the supersonic combustion in aircraft engines [1] and the inertial confinement fusion (ICF) [2], [3]. The flow pattern is diverse and the dynamical interactions of phases separated by a free surface significantly complicate the mathematical description of the inherently multi-component flow problem. The propagation of a shock wave through this type of inhomogeneous media leads to baroclinic vorticity generation and the development of the Richtmyer-Meshkov instability (RMI) [4]. This hydrodynamic instability grows nonlinearly and subsequently shows transition to turbulence without any wall effects. Vorticity generation is proportional to the misalignment between the density gradient at the fluid interface and induced upstream-directed pressure gradients related to a shock wave.

Numerous experiments have been carried out to investigate the initial stages of this process. The interaction of a planar shock wave with a single spherical or cylindrical bubble has been a typical experimental setup chosen to study the interface perturbation and deformation. The studies have been performed using shadowgraph diagnostic techniques as in the work of Haas & Sturtevant [5] and the series of experiments of Layes *et al*, see for example [6]. The other experiments applied modern laser technologies [7]. All these experiments allowed for better understanding of the mechanism of the

[1] To whom any correspondence should be addressed.

shock-bubble interaction and provided the reference data for computational studies, which have been performed using different mathematical models and numerical methods.

For the purpose of this study a diffuse interface approach has been developed to mathematically represent and numerically simulate flows with interfaces separating components of various density ratios. The method considers interfaces as numerically diffused zones, taking advantage of inherent numerical diffusion. This is in contrast to other approaches that consider interfaces between flow components as sharp non-smeared discontinuities, see for example [8]. The formulation is based on the model known, in its one-dimensional form, as the six-equation model of Saurel *et al* [9]. It was first derived by Kapila *et al* [10] from the generic model of Baer and Nunziato [11]. A brief introduction of the model as well as of the numerical method is provided in the next sections. This is followed by the general description of the mechanism of vorticity generation, the numerical results and conclusions.

2. Multi-component flow model

The original six equation model formerly derived by [10] in one dimensional space is now considered in two dimensional space. It consists of a statistical volume fraction equation, two continuity equations, mixture momentum equation in x and y direction and two energy equations. This model is characterized by two pressures attributed to each phase and a single velocity. It is therefore considered as a pressure non-equilibrium model, which requires further relaxation. Therefore, its solution discussed in the following section is based on a predictor-corrector, Godunov-type method and a diffuse-interface approach for the material interfaces. The model for compressible flows without mass and heat transfer can be reduced to:

$$
\begin{aligned}
&\frac{\partial \alpha_1}{\partial t} + u\frac{\partial \alpha_1}{\partial x} + v\frac{\partial \alpha_1}{\partial y} = \mu(p_1 - p_2),\\
&\frac{\partial \alpha_1\rho_1}{\partial t} + \frac{\partial \alpha_1\rho_1 u}{\partial x} + \frac{\partial \alpha_1\rho_1 v}{\partial y} = 0,\\
&\frac{\partial \alpha_2\rho_2}{\partial t} + \frac{\partial \alpha_2\rho_2 u}{\partial x} + \frac{\partial \alpha_2\rho_2 v}{\partial y} = 0,\\
&\frac{\partial \rho u}{\partial t} + \frac{\partial [\rho u^2 + (\alpha_1 p_1 + \alpha_2 p_2)]}{\partial x} + \frac{\partial \rho uv}{\partial y} = 0,\\
&\frac{\partial \rho v}{\partial t} + \frac{\partial \rho uv}{\partial x} + \frac{\partial [\rho v^2 + (\alpha_1 p_1 + \alpha_2 p_2)]}{\partial y} = 0,\\
&\frac{\partial \alpha_1\rho_1 e_1}{\partial t} + \frac{\partial \alpha_1\rho_1 e_1 u}{\partial x} + \frac{\partial \alpha_1\rho_1 e_1 v}{\partial y} + \alpha_1 p_1\frac{\partial u}{\partial x} + \alpha_1 p_1\frac{\partial v}{\partial y} = -p_i\mu(p_1 - p_2),\\
&\frac{\partial \alpha_2\rho_2 e_2}{\partial t} + \frac{\partial \alpha_2\rho_2 e_2 u}{\partial x} + \frac{\partial \alpha_2\rho_2 e_2 v}{\partial y} + \alpha_2 p_2\frac{\partial u}{\partial x} + \alpha_2 p_2\frac{\partial v}{\partial y} = p_i\mu(p_1 - p_2),
\end{aligned}
\qquad (1)
$$

where α_k, ρ_k, p_k, e_k, ρ, u, v and p are the volume fraction, the density, the pressure, the specific internal energy of the phase k, the mixture density, mixture velocity components and mixture pressure, respectively. The variable μ is a homogenization parameter controlling the rate at which the pressure tends towards equilibrium. An additional equation has been derived by [9] and considered in the numerical solution of the model (1) to eliminate the errors in the values of the thermodynamic variables due to the numerical approximation of the two non-conservative internal energy equations in the presence of shocks. This equation is obtained by summing up the two internal energy equations with mass and momentum equations and takes the following final form:

$$
\frac{\partial \rho E}{\partial t} + \frac{\partial u(\rho E + \alpha_1 p_1 + \alpha_2 p_2)}{\partial x} + \frac{\partial v(\rho E + \alpha_1 p_1 + \alpha_2 p_2)}{\partial y} = 0, \qquad (2)
$$

where the mixture total energy is given by:

$$E = \frac{\alpha_1\rho_1}{\rho} e_1 + \frac{\alpha_2\rho_2}{\rho} e_2 + \frac{1}{2}u^2 + \frac{1}{2}v^2, \tag{3}$$

The stiffened gas equation of state relates the thermodynamic variables and has the following form:

$$p_k = (\gamma_k - 1)\rho_k e_k - \gamma_k \pi_k, \tag{4}$$

where γ_k and π_k are respectively the heat capacity ratio and the pressure constant for the phase k.The stiffened equation of state for the mixture can be written in the following compact form:

$$p = \frac{\rho e - \sum_k^2 (\frac{\alpha_k \gamma_k \pi_k}{\gamma_k - 1})}{\sum_k^2 (\frac{\alpha_k}{\gamma_k - 1})}. \tag{5}$$

3. Numerical method

The model (1) is hyperbolic but non-conservative, i.e. it cannot be written in the divergence form. Therefore the standard numerical methods developed for solving the hyperbolic conservation laws are not applied directly. In order to solve the model (1) the usual numerical procedure is to decompose the governing equations into hyperbolic and relaxation parts and solve them in succession of operations. The hyperbolic part of the model (1) can be rewritten as:

$$\begin{aligned}
&\frac{\partial \alpha_1}{\partial t} + u\ \frac{\partial \alpha_1}{\partial x} + v\frac{\partial \alpha_1}{\partial y} = 0,\\
&\frac{\partial \alpha_1\rho_1 e_1}{\partial t} + \frac{\partial \alpha_1\rho_1 e_1 u}{\partial x} + \frac{\partial \alpha_1\rho_1 e_1 v}{\partial y} + \alpha_1 p_1 \frac{\partial u}{\partial x} + \alpha_1 p_1 \frac{\partial v}{\partial y} = 0,\\
&\frac{\partial \alpha_2\rho_2 e_2}{\partial t} + \frac{\partial \alpha_2\rho_2 e_2 u}{\partial x} + \frac{\partial \alpha_2\rho_2 e_2 v}{\partial y} + \alpha_2 p_2 \frac{\partial u}{\partial x} + \alpha_2 p_2 \frac{\partial v}{\partial y} = 0,\\
&\frac{\partial U}{\partial t} + \frac{\partial F(U)}{\partial x} + \frac{\partial G(U)}{\partial y} = 0,
\end{aligned} \tag{6}$$

where the conserved variables U and the fluxes $F(U)$ and $G(U)$ are given in a vector form as:

$$U = \begin{bmatrix} \alpha_1\rho_1 \\ \alpha_2\rho_2 \\ \rho u \\ \rho v \\ \rho E \end{bmatrix},\ F(U) = \begin{bmatrix} \alpha_1\rho_1 u \\ \alpha_2\rho_2 u \\ \rho u^2 + p \\ \rho uv \\ u(\rho E + p) \end{bmatrix} \quad \text{and} \quad G(U) = \begin{bmatrix} \alpha_1\rho_1 v \\ \alpha_2\rho_2 v \\ \rho uv \\ \rho v^2 + p \\ v(\rho E + p) \end{bmatrix}. \tag{7}$$

The elements in the last row of the above vectors in (7) represent the additional equation of the total mixture energy (2). The hyperbolic part (6) is solved using a Godunov-type scheme. The explicit first-order Godunov scheme can be written as:

$$\begin{aligned}
U_{i.j}^{n+1} = U_{i,j}^n &- \frac{\Delta t}{\Delta x}[F(U^*(U_{i,j}^n, U_{i+1,j}^n)) - F(U^*(U_{i-1,j}^n, U_{i,j}^n))]\\
&- \frac{\Delta t}{\Delta y}[G(U^*(U_{i,j}^n, U_{i,j+1}^n)) - G(U^*(U_{i,j-1}^n, U_{i,j}^n))].
\end{aligned} \tag{8}$$

Equation (8) is applied to the mass, momentum and total energy equations, where the superscript * in (8) refers to the state at cell boundaries. The discretisation of the non-conservative equation for the volume fraction is:

$$\alpha_{1i,j}^{n+1} = \alpha_{1i,j}^{n} - \frac{\Delta t}{\Delta x} u_{i,j}[(u\alpha_1)^{*}_{i+1/2,j} - (u\alpha_1)^{*}_{i-1/2,j} - \alpha_{1i,j}^{n}(u^{*}_{i+1/2,j} - u^{*}_{i-1/2,j})] - \frac{\Delta t}{\Delta y} v_{i,j}[(v\alpha_1)^{*}_{i,j+1/2} - (v\alpha_1)^{*}_{i,j-1/2} - \alpha_{1i,j}^{n}(v^{*}_{i,j+1/2} - v^{*}_{i,j-1/2})]. \quad (9)$$

The non-conservative equations for the internal energy are discretised as follows:

$$(\alpha\rho e)_{ki,j}^{n+1} = (\alpha\rho e)_{ki,j}^{n} - \frac{\Delta t}{\Delta x} u_{i,j}[(\alpha\rho eu)^{*}_{ki+1/2,j} - (\alpha\rho eu)^{*}_{ki-1/2,j} - (\alpha p)_{ki,j}^{n}(u^{*}_{i+1/2,j} - u^{*}_{i-1/2,j})] - \frac{\Delta t}{\Delta y} v_{i,j}[(\alpha\rho ev)^{*}_{ki,j+1/2} - (\alpha\rho ev)^{*}_{ki,j-1/2} - (\alpha p)_{ki,j}^{n}(v^{*}_{i,j+1/2} - v^{*}_{i,j-1/2})] \quad (10)$$

In the present work the second order accuracy is achieved by using the MUSCL scheme. The HLL approximate Riemann solver is employed to calculate the numerical fluxes.

When the hyperbolic part of the solution algorithm is accomplished, the pressure is modified by relaxation solver based on the instantaneous pressure relaxation assumption, where the variable μ for this purpose is considered to be infinite. This part of the solution requires an iterative procedure to solve the ordinary differential equations containing the source terms of the original model (1):

$$\frac{\partial}{\partial t}\begin{bmatrix} \alpha_1 \\ \alpha_1\rho_1 \\ \alpha_2\rho_2 \\ \rho u \\ \rho v \\ \alpha_1\rho_1 e_1 \\ \alpha_2\rho_2 e_2 \end{bmatrix} = \begin{bmatrix} \mu(p_1 - p_2) \\ 0 \\ 0 \\ 0 \\ 0 \\ -\mu p_i(p_1 - p_2) \\ \mu p_i(p_1 - p_2) \end{bmatrix} \quad (11)$$

The new value of pressure resulting in the updated value of the volume fraction and the mixture energy ρe calculated from (2) are used to obtain the mixture pressure from the mixture equation of state (5). The new pressure can be now used to update the internal energies for each constituent with the help of the corresponding equations of state.

4. Mechanism of vorticity generation

The acceleration of a gas bubble by a plane shock wave causes a number of complex phenomena such as bubble compression and acceleration, interface instabilities and vorticity generation. The main source of vorticity generation in such cases is the misalignment of the pressure and the density gradients, which is known as the baroclinic vorticity deposition. Figure 1 shows a schematic diagram of the possible scenarios when a planar shock wave propagating initially in air passes through a heavier or lighter cylindrical gas bubble. To explain the evolution of the vorticity field, it is convenient to consider Euler equations written in a vorticity transport form. In 2D form the equation is:

$$\frac{D\omega}{Dt} = -\omega(\nabla \cdot U) + \frac{1}{\rho^2}(\nabla\rho \times \nabla p) \quad (12)$$

The only term of importance in the early stages of a shock-bubble interaction for which ω is initially equal to zero is the baroclinic torque ($\nabla\rho \times \nabla p$). The misalignment of the local pressure and density gradients leads to the non-zero source term in equation (12). The baroclinic torque is the largest if the pressure gradient is perpendicular to the density gradient. Whereas, at the most upstream and downstream poles of the gas bubble, the baroclinic torque is equal to zero, owing to the collinearity of density and pressure gradients. The curvature of the shock wave front (the refracted shock wave) has also been used to build a theory behind the vorticity generation This mechanism is based on the conservation of the tangential velocity and the angular momentum across the shock wave as the compression only affects the motion normal to the shock surface (for details see [12] and [13]).

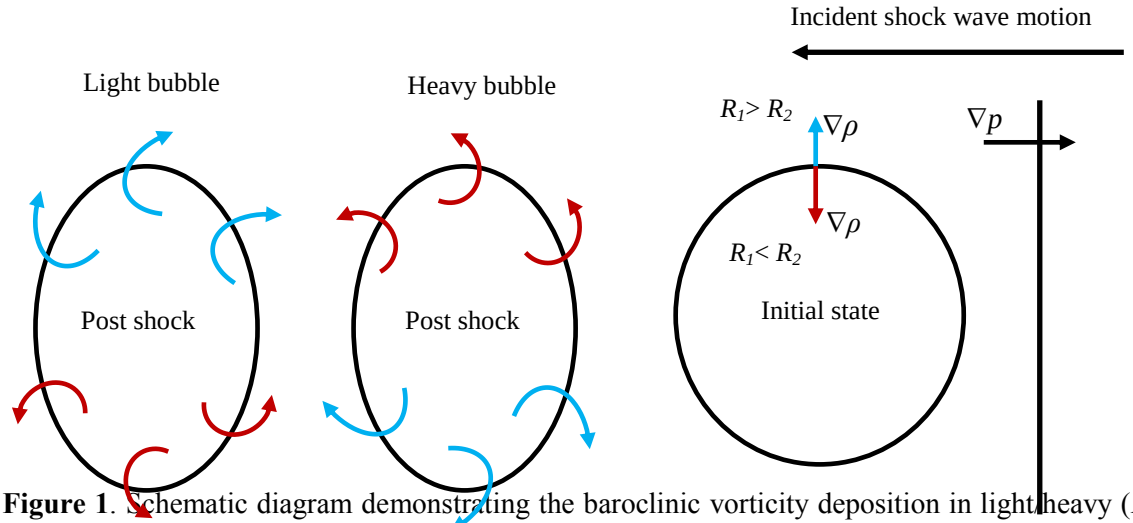

Figure 1. Schematic diagram demonstrating the baroclinic vorticity deposition in light/heavy ($R_1 < R_2$) and heavy/light ($R_1 > R_2$) shock-bubble interaction scenarios. R_1 is the acoustic impedance of the air and R_2 refers to the acoustic impedance of the bubble.

5. Numerical results

Numerical simulations of different scenarios of the interaction of a planar shock wave propagating in the ambient air and encountering a single circular bubble are conducted. Three air/bubble arrangements that represent heavy/light, equal density and light/heavy are considered. The configurations include air/krypton (Kr), air/nitrogen (N_2) and air/helium (He), which represent negative, close to zero and positive Atwood number A respectively. The Atwood number is expressed in terms of density ratio as follows:

$$A = \frac{(\rho_b - \rho_s)}{(\rho_b + \rho_s)} \qquad (13)$$

where, ρ_b and ρ_s are the densities of the gas filling the bubble and the surrounding medium respectively. The simulations consider shock waves of Mach numbers (M = 1.5, 1.7 and 2.0). The physical domain and the initial conditions are illustrated in figure 2 and tables 1 and 2.

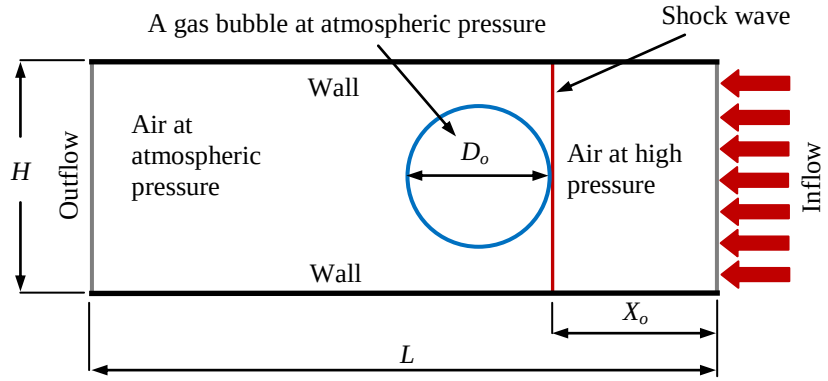

Figure 2. Schematic diagram of the initial state of shock-bubble interaction simulations.

Table 1. Initial conditions of air and different gas bubbles in the pre-shock chamber.

Physical Property	**Air**	**He**	**N_2**	**Kr**
Density, kg/m^3	1.29	0.167	1.25	3.506
Pressure, Pa	101325	101325	101325	101325
Horizontal velocity, m/s	0.0	0.0	0.0	0.0
Vertical velocity, m/s	0.0	0.0	0.0	0.0
Sound speed, m/s	332	1005	337	220
Heat capacity ratio γ	1.4	1.67	1.4	1.67

Table 2. Initial conditions of air in the post-shock chamber.

Physical Property	***M* = 1.5**	***M* = 1.7**	***M* = 2**
Density, kg/m^3	2.4021	2.835	3.44
Pressure, Pa	249091	324747	455963
Horizontal velocity, m/s	230.28	374.55	414.5
Heat capacity ratio, γ	1.4	1.4	1.4

The characteristic dimensions of the domain as shown in figure 2 are: L = 30 cm, H = 8 cm, X_o = 5 cm and D_o = 4 cm. The initial and boundary conditions of these computational cases reflect the experimental setup of Layes and Le Métayer [14]. The present computations were performed using 1800 × 480 computational cells. The Schlieren images of the structures obtained in the experiment and computational simulations are in good agreement. Although it has to be remembered that the experiments involves a spherical bubble and the computational results are restricted to the cylindrical bubble. The results of the interface evolution as a function of time for the different air/gas bubble arrangements are shown in figure 3 for the M = 1.5.

The left plots in figure 3 show the evolution of the Kr bubble interface. The initial Atwood number is 0.462 and this case represents light/heavy arrangement. After the planar shock wave impacts the Kr bubble, a refracted shock propagates inside the bubble, the outer parts of the incident shock propagate outside the bubble and a reflected shock propagates back towards the right side. The acoustic impedance inside the bubble is higher than the acoustic impedance outside ($R_2 > R_1$). This causes the refracted shock wave, inside the bubble to travel more slowly than the incident shock outside the bubble, figure 3 at time 47 μs. A sheet of positive vorticity along the upper surface and another sheet of negative vorticity along the lower surface correspond to the interface formed behind the shock wave. By the time 166 μs the vortices on the top and bottom of the bubbles become more visible and a penetrating jet is formed at the downstream pole of the Kr bubble. As the time goes the vortical flow dominates the interface deformation process.

The middle plots in figure 3 present the interaction of a planar shock wave with N_2 bubble. The Atwood number in this case is close to zero and the difference in the acoustic impedance is small. In this case the speed difference of the refracted shock wave and the incident shock wave is small as it can be seen in figure 3. The N_2 bubble undergoes a compression process, and the vorticity production in this case is negligible.

The right plots in figure 3 show the snapshots of the interaction of a shock wave with the He bubble. The case represents an opposite scenario to the case of the Kr bubble. In this experiment the Atwood number is equal to -0.77 which is representative to the heavy/light arrangement. The shock wave hits the right interface of the He bubble causing a refracted shock wave to propagate inside the bubble faster than the incident shock wave outside the bubble, as a result of the acoustic impedance

misalignment (in this scenario $R_2 < R_1$). In this scenario a rarefaction wave reflects and propagates back towards the right side. The bubble interface deforms and a penetrating jet acting along the line of symmetry in the main flow direction is formed. The upstream pole of the bubble moves towards the downstream one and the bubble interface evolves into a kidney shape.The penetrating high velocity jet along the flow direction moves through the bubble forming symmetric patterns, figure 3. When the bubble deforms the associated flow field is subsequently split into two rings of vorticity.

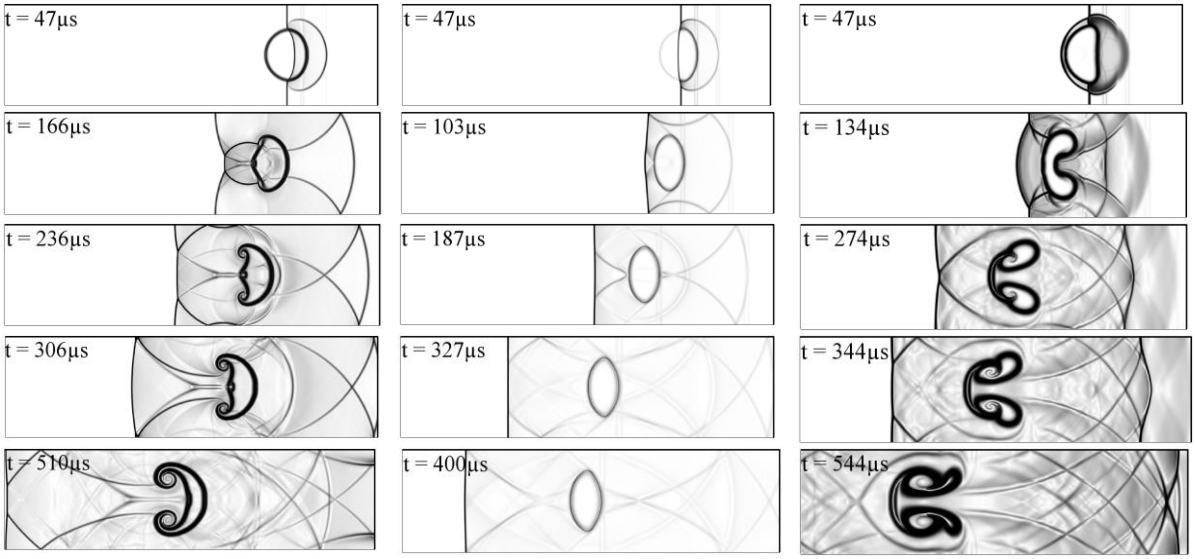

Figure 3. Numerical Schlieren images of the mixture density contours representing the interface evolution with respect to time for air/Kr (left), air/N_2 (centre) and air/He (right) at M = 1.5.

The intensity of the vortex rings in the cases of He and Kr bubbles is expressed by the total circulation Γ. The calculated values of the circulation in the symmetrical half of the computational domain with respect to time are represented in figure 4 for all Mach numbers considered. The values of the circulation show that: if the Mach number increases the values of the circulation also increase and their growth rate during the shock-bubble interaction process is increased too. In the case of the relatively high absolute values of the Atwood number the vorticity generation becomes higher as well.

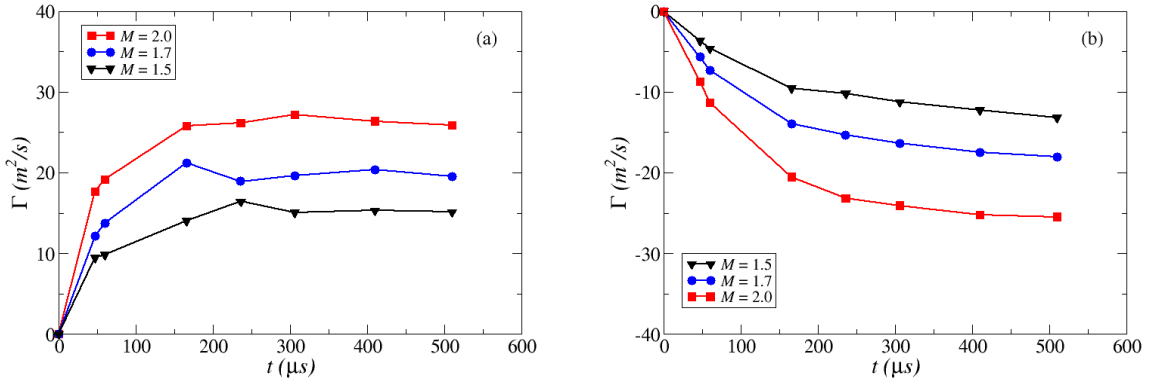

Figure 4. Circulation time evolution of air/He (a) and air/Kr (b) constitutions for different shock wave celerities.

6. Conclusions

Numerical simulations were performed to capture vorticity generation and the interface evolution in multi-component compressible flows. The study considered the effect of Atwood and Mach numbers on vorticity generation resulting from the interaction of a planar shock wave with a single cylindrical bubble. The constant Mach number comparison demonstrated that an increase of the Atwood number leads to a higher vorticity generation and its effect on the interface evolution becomes more pronounced. The constant Atwood number comparison proved that the flow with increasing Mach number produces higher circulation and vorticity generation.

7. References

[1] Yang J, Kubota T and Zukoski E E 1993 Applications of shock-induced mixing to supersonic combustion *AIAA Journal* **31** pp 854-862

[2] Lindl J D, McCrory R L and Campbell E M 1992 Progress toward ignition and burn propagation in inertial confinement fusion *Physics Today* **45** pp 32-40

[3] Aglitskiy Y; Velikovich A L; Karasik M; Metzler N; Zalesak S T; Schmitt A J; Phillips L; Gardner J H; Serlin V; Weaver J L and Obenschain S P 2010 Basic hydrodynamics of Richtmyer-Meshkov-type growth and oscillations in the inertial confinement fusion-relevant conditions *Philosophical Transactions of the Royal Society A: Mathematical,Physical and Engineering Sciences* **368** pp 1739-1768

[4] Brouillette M 2002 The Richtmyer-Meshkov instability *Annual Review of Fluid Mechanics* **181** 41

[5] Haas J and Sturtevant B 1987 Interaction of weak shock waves with cylindrical and spherical gas inhomogeneities *Journal of Fluid Mechanics* **181** pp 41-76

[6] Layes G, Jourdan G and Houas L 2009 Experimental study on a plane shock wave accelerating a gas bubble *Physics of Fluids* **21** 074102

[7] Ranjan D, Niederhaus J, Motl B, Anderson M, Oakley J and Bonazza R 2007 Experimental investigation of primary and secondary features in high Mach number shock-bubble interaction *Physical Review Letters* **98** 024502

[8] Terashima H and Tryggvason G 2009 A front-tracking/ghost-fluid method for fluid interfaces in compressible flows. *Journal of Computational Physics* **228** pp 4012–4037

[9] Saurel R, Petitpas F and Berry R A 2009 Simple and efficient relaxation methods for interfaces separating compressible fluids, cavitating flows and shocks in multiphase mixtures *Journal of Computational Physics* **228** pp 1678–1712

[10] Kapila A K, Menikoff R, Bdzil J B, Son S F and Stewart D S 2001 Two-phase modeling of deflagration to detonation transition in granular materials: Reduced equations *Physics of Fluids* **13** pp 3002-3024

[11] Baer M K and Nunziato J W 1986 A two-phase mixture theory for the deflagration-to-detonation transition (DDT) in reactive granular materials *International Journal of Multiphase Flow* **12** 861-888

[12] Kevlahan N K -R 1997 The vorticity jump across a shock in a non-uniform flow *Journal of Fluid Mechanics* **341** pp 371-384

[13] Huete Ruiz de Lira C, Velikovich A L and Wouchuk J G 2011 Analytical linear theory for the interaction of a planar shock wave with a two or three-dimensional random isotropic density field *Physical Review E* **83** 056320

[14] Layes G and Le Métayer O 2007 Quantitative numerical and experimental studies of the shock accelerated heterogeneous bubbles motion *Physics of Fluids* **19** 042105